Optical damage thresholds of single-mode fiber-tip spintronic terahertz emitters

Felix Paries, Felix Selz, Jean-Francois Lampin, Pierre Kolejak, Geoffrey Lezier, Nicolas Tiercelin, Mathias Vanwolleghem, Tobias Kampfrath, Tom Seifert, Georg von Freymann, et al.

▶ **To cite this version:**

Felix Paries, Felix Selz, Jean-Francois Lampin, Pierre Kolejak, Geoffrey Lezier, et al.. Optical damage thresholds of single-mode fiber-tip spintronic terahertz emitters. 2024. hal-04601846

HAL Id: hal-04601846
https://hal.science/hal-04601846

Preprint submitted on 5 Jun 2024

HAL is a multi-disciplinary open access archive for the deposit and dissemination of scientific research documents, whether they are published or not. The documents may come from teaching and research institutions in France or abroad, or from public or private research centers.

L'archive ouverte pluridisciplinaire **HAL**, est destinée au dépôt et à la diffusion de documents scientifiques de niveau recherche, publiés ou non, émanant des établissements d'enseignement et de recherche français ou étrangers, des laboratoires publics ou privés.

Optical damage thresholds of single-mode fiber-tip spintronic terahertz emitters

FELIX PARIES,[1,2,*] FELIX SELZ,[1,2] JEAN-FRANÇOIS LAMPIN,[3] PIERRE KOLEJÁK,[3,4] GEOFFREY LEZIER,[3] NICOLAS TIERCELIN,[3] MATHIAS VANWOLLEGHEM,[3] TOBIAS KAMPFRATH,[5] TOM S. SEIFERT,[5,6] GEORG VON FREYMANN,[1,2] AND DANIEL MOLTER[1]

[1]*Fraunhofer Institute for Industrial Mathematics ITWM, Department Materials Characterization and Testing, 67663 Kaiserslautern, GERMANY*
[2]*Department of Physics and Research Center OPTIMAS, RPTU Kaiserslautern-Landau, 67663 Kaiserslautern, GERMANY*
[3]*University of Lille, CNRS, Centrale Lille, Université Polytechnique Hauts-de-France, UMR 8520 - IEMN, 59000 Lille, FRANCE*
[4]*IT4Innovations & Faculty of Materials Science and Technology, VSB-Technical University of Ostrava, 708 00 Ostrava, CZECH REPUBLIC*
[5]*Department of Physics, Freie Universität Berlin, 14195 Berlin, GERMANY*
[6]*TeraSpinTec GmbH, Lüneburger Str. 26, 10557 Berlin, GERMANY*
[*]*felix.paries@itwm.fraunhofer.de*

Abstract: Spintronic terahertz emitters (STEs) are gapless, ultrabroadband terahertz sources that can be driven within a wide pump-wavelength and repetition-rate range. While STEs driven by strong pump lasers operating at kilohertz repetition rates excel in generating high electric field strengths for terahertz spectroscopy or ellipsometry, newly advancing technologies such as ultrafast modulation of terahertz polarization, scanning tunneling microscopy, laser terahertz emission nanoscopy, and fully fiber-coupled integrated systems demand an STE pumping at megahertz repetition rates. In all these applications the available terahertz power is ultimately limited by the STE's optical damage threshold. However, to date, only very few publications have targeted this crucial topic and investigations beyond the kilohertz repetition-rate regime are missing.

Here, we present a complete study of our single-mode fiber-tip STEs' optical damage thresholds covering the kilohertz, megahertz, and gigahertz repetition-rate regimes as well as continuous-wave irradiation. As a very important finding, we introduce the necessity of classifying the optical damage threshold into two regimes: a low-repetition-rate regime characterized by a nearly constant fluence threshold, and a high-repetition-rate regime characterized by an antiproportional fluence dependence ("average-power threshold"). For our single-mode fiber-tip STEs, the transition between these regimes occurs around 4 MHz.

Moreover, we present a cohesive theory of the damaging thermodynamical processes at play and identify temperature-driven inter-layer diffusion as the primary cause of the STE failure. These findings are substantiated by atomic force microscopy, infrared scattering-type scanning near-field optical microscopy, and scanning transmission electron microscopy measurements.

This new level of understanding offers a clear optimization lever and provides valuable support for future advancements in the promising field of spintronic terahertz emission.

© 2024 Optica Publishing Group

1. Introduction

Over the last decades, a variety of different terahertz emitters have been developed. A useful classification divides them into two main classes: (1) those based on off-resonant charge motion within nonlinear media of broken inversion symmetry ("optical rectification") [1, 2] such as inorganic crystals [3] or suitable organic materials [4], and (2) those based on resonantly induced photocurrents such as photoconductive antennas [5–8], laser-ionized gases and liquids [9–13], or the recently developed spintronic terahertz emitters (STEs) [14–18].

STEs are based on the down conversion of an ultrashort laser pulse into an ultrabroadband terahertz pulse through a sequence of spin-current generation, spin-to-charge conversion, and current-to-field conversion. Due to their simple metallic thin-film-stack design, they can be sputtered onto various substrates and, thus, be fabricated and scaled at low cost. The metallic nature in combination with an excess-energy-induced terahertz spin voltage [19] enables the STEs to be pumped across a broad wavelength range encompassing terahertz [20], infrared [21], visible [22], and ultraviolet [23], which makes them a very versatile class of terahertz emitters. Moreover, their emission was shown to cover the full terahertz range without any spectral gaps outperforming all terahertz emitter classes except laser-ionized gases in terms of bandwidth [24]. However, in contrast to laser-ionized gases, STEs do not necessarily require pulse energies on the order of hundreds of microjoules to photo-ignite a plasma [17] but can be operated at pulse energies in the picojoule regime. To compete with the traditional emitter classes in terms of generated terahertz power and electric field strength, large-area STEs are used. Using a beam expander in combination with appropriate thermal management, terahertz pulses with peak electric fields above 1.5 MV/cm and fluences above 1 mJ/cm^2 were achieved offering a promising alternative to traditional $LiNbO_3$-crystals as a high-field source [25].

As all solid-state-terahertz emitters, STEs are subject to material destruction if a specific pump-fluence or average-pump-power-density threshold is exceeded. This property becomes a major challenge in applications where either a high electric field strength or a small beam diameter is required.

However, to date, only two studies have targeted this crucial challenge of optical damage threshold. Both of them, by Kumar et al. (1 kHz, 4-8 mJ/cm^2) [26] and Vogel et al. (100-400 kHz, 4-5 mJ/cm^2) [27], addressed repetition rates below 400 kHz. To the best of the authors' knowledge, the optical damage behavior at repetition rates above 400 kHz has not been investigated in detail yet, even though it is of crucial importance for many recently emerging STE applications such as ultrafast modulation of terahertz polarization [28,29], scanning tunneling microscopy (STM) [30], laser terahertz emission nanoscopy (LTEN) [31], inverse-spin-Hall photomixing [32], and fully fiber-coupled integrated systems [33].

Here, we reveal the necessity of classifying the optical damage threshold into two regimes: a high-peak-power, low-repetition-rate regime characterized by a nearly constant fluence threshold, and a low-peak-power, high-repetition-rate regime characterized by an antiproportional fluence dependence ("average-power threshold"). Taking advantage of our recently developed single-mode fiber-tip STEs, where the pump field is guaranteed to be nearly identical for every sample due to its waveguiding nature, we were able to characterize the optical damage threshold with high accuracy. Covering a repetition-rate range from 200 kHz to 1 GHz as well as continuous-wave irradiation, we could reveal a transition from the constant-fluence-threshold regime to the average-power-threshold regime at approximately 4 MHz.

Moreover, using atomic force microscopy (AFM), infrared scattering-type scanning near-field optical microscopy (s-SNOM), and scanning transmission electron microscopy (STEM) measurements, we found temperature-driven inter-layer diffusion to be the responsible damage mechanism restricting the optical-to-terahertz-conversion processes.

2. Methods

2.1. Fabrication

The spintronic W(2.0 nm) / FeCoB(1.8 nm) / Pt(2.0 nm) tri-layer structure was deposited on the fiber tips using a thin-film sputtering process. Prior to deposition, a cleaning procedure involved ultrasonication in successive baths of acetone (30 s), isopropyl alcohol (120 s), and de-ionized water (120 s). The W/FeCoB/Pt spintronic emitters were deposited by RF-diode sputtering in LEYBOLD Z550 equipment where the individual layers are sputtered from circular 4-inch targets. In particular, the $Fe_{60}Co_{20}B_{20}$ alloy is obtained from a target with this stoichiometry. To ensure high precision in the thicknesses, the deposition was carried on a rotatory turn-table substrate holder in an oscillation mode: each time the substrate passes under the target, which corresponds to one oscillation, a layer of the material is deposited with a thickness that depends on the angular speed of the turn-table. The deposition is carefully calibrated beforehand by depositing a film with 100 oscillations.

2.2. Method of inflicting damage

To precisely measure the optical damage threshold with statistical significance, we destroyed more than 30 single-mode fiber-tip STEs by intentionally exceeding the pump threshold. Due to the waveguiding nature of the single-mode glass fibers, the pump field is guaranteed to be nearly identical for every sample. This removes the mode field area as a free parameter and allows calculating the fluence accurately with only the irradiance to be measured. The irradiance has been controlled via a suitable combination of pump current and attenuation.

Fig. 1 a) illustrates the damage setup consisting of an erbium-doped fiber laser (EDFL), an erbium-doped fiber amplifier (EDFA), and a fiber-tip STE sample. The fiber-tip STEs are butt-coupled to the pump fiber via a standard FC/PC fiber connection and an index-matching gel is used to minimize reflection losses at the interface. Additionally, the transmittance is carefully monitored to ensure identical initial conditions for each sample. The repetition-rate dependence of the optical damage threshold is investigated by employing four EDFL systems operating at around 1550 nm. These systems cover the repetition-rate range from 200 kHz to 1 GHz as well as continuous-wave irradiation (0.2-80 MHz: *in-house EDFL + APE pulseSelect*, 100 MHz: *Menlo ELMO*, 1 GHz: *Menhir 1550*, CW: *Yenista Optics Tunics T100S-HP*).

Fig. 1 b) depicts the damage method: each fiber-tip STE sample is irradiated for 2 minutes at each pump stage (0 - 10 mW, 1 mW step size). The material damage is monitored between the pump stages at a reference level 1 mW below the threshold and during each pump stage.

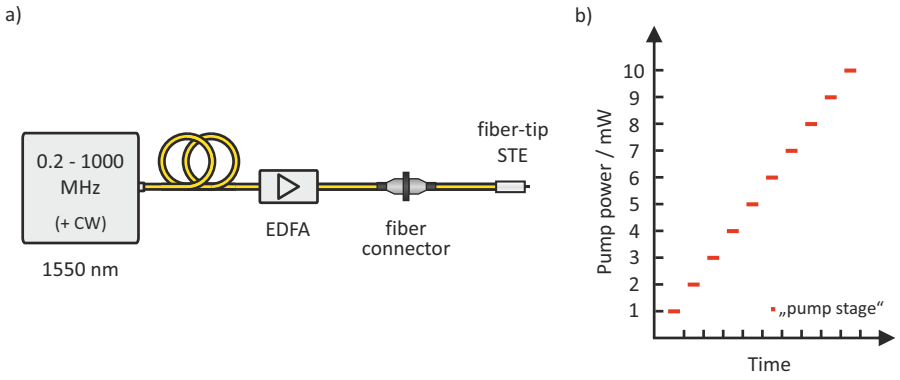

Fig. 1. Method of inflicting damage. a) The single-mode fiber-tip STE is damaged by intentionally exceeding the pump threshold. To cover a broad repetition-rate range from 0.2-1000 MHz (+CW), various erbium-doped fiber laser systems with a central wavelength around 1550 nm have been employed. More than 30 fiber-tip STEs have been destroyed to achieve statistical significance. b) Each of the samples underwent a ramp with 2 minutes of irradiation at each pump stage. Between and during each pump stage, damage-detection measurements have been conducted.

2.3. Methods of detecting damage

To detect and investigate the optical damage thresholds of our single-mode fiber-tip STEs, we employed three different detection methods: (a) terahertz-amplitude detection, (b) optical-microscopy detection, and (c) infrared-transmittance detection. These are illustrated in Fig. 2.

2.3.1. Terahertz-amplitude detection

As will be seen in the results, the pump-induced material damage is accompanied by an irreversible drop in infrared-to-terahertz conversion efficiency. Thus, recording the temporal evolution of the terahertz peak-to-peak amplitude in the time domain for each pump stage provides the most direct damage measure. We acquired this measure for two identically fabricated fiber-tip STEs exemplary using a standard delay-line-based terahertz time-domain spectroscopy setup at 100 MHz repetition rate (Fig. 2 a)). However, these terahertz measurements are error-prone due to a relatively weak signal-to-noise ratio and the adaptation to the low repetition-rate regime is not straightforward especially as the damage threshold of the used photoconductive detector may be exceeded. Consequently, we switched to equivalent damage measures accessible in the visible and near-infrared where the high photon energy allows for robust and highly sensitive detection via the photo effect.

2.3.2. Optical-microscopy detection

Since the pump-induced material damage coincides with a visible darkening of the material, it is possible to monitor the damage with commercially available optical microscopes for fiber inspection. Consequently, we took a microscopy image after each 2-minute pump stage and quantified the darkening using a self-developed imaging analysis software that determines the degree of darkening based on the taken images. This turned out to be a highly sensitive method. However, it requires considerable analysis effort.

2.3.3. Infrared-transmittance detection

Since the pump-induced material damage is accompanied by an increase in infrared transmittance, very accurate commercially available infrared power meters can be used to observe the damage. We used a Germanium-based photodiode with a resolution of 2 nW (Thorlabs S122C) to monitor the transmittance between the pump stages at a chosen reference level as well as during each pump stage. This turned out to be an excellent method combining both high simplicity and high sensitivity.

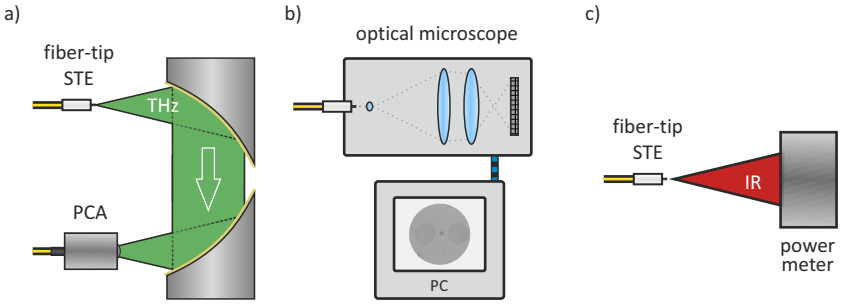

Fig. 2. Damage-detection methods. a) A conventional single-laser terahertz time-domain spectroscopy (TDS) setup with an interferometrically monitored mechanical delay line is used to measure the terahertz waveforms. The terahertz peak-to-peak amplitude serves as a damage measure. b) The fiber-tip STEs' end facets are imaged with a commercially available fiber-inspection microscope. The darkening is quantified by self-developed image analysis software within the region of the fiber core. c) The infrared transmittance is measured using a Germanium-based high-resolution photodiode.

3. Results

3.1. Terahertz-amplitude detection

Fig. 3 a) shows the terahertz peak-to-peak amplitude measured for two single-mode fiber-tip STEs after each pump stage at a reference level of 4 mW. With increasing pump stages, the terahertz peak-to-peak amplitude decreases irreversibly. Fig. 3 b) displays the amplitude's temporal evolution during a 4 mW and a 5 mW irradiation interval. At 5 mW, the terahertz peak-to-peak amplitude decreases irreversibly by 10 percent over an irradiation period of 2 minutes. At 4 mW, the decrease, if any, is found to be minor. Consequently, the derived damage threshold is 5 mW corresponding to an average-pump-power density of 4.8 kW/cm^2.

3.2. Optical-microscopy detection

Fig. 4 shows three images of a continuous-wave-irradiated single-mode fiber-tip STE with different degrees of destruction. After two minutes of continuous-wave irradiation at 4 mW, the sample does not show any darkening within the fiber's core area. However, after consecutive two-minute irradiation periods at 4, 5, 6, and 7 mW, a subtle darkening becomes apparent. Continuing the destruction procedure, the darkening increases and the dark spot becomes highly pronounced. Using self-developed imaging analysis software, we quantified this darkening based on the mean change of the 8-bit grayscale value within the region of the fiber's core.

Fig. 5 displays this quantified darkening after each pump stage averaged over three continuous-wave-irradiated samples. The error bars illustrate the standard deviation.

3.3. *Infrared-transmittance detection*

The blue markers in Fig. 5 illustrate the relative change of infrared transmittance at the end of each pump stage. The results are in excellent quantitative agreement with the darkening data verifying the interchangeability of these two methods. Moreover, the damage thresholds were found to be identical to those derived from the terahertz-amplitude detection. Thus, for the subsequent measurements, we decided to detect solely in the infrared since it is the simplest and least error-prone method. The threshold value is determined by pinpointing the average optical power where the infrared transmittance increased by at least 10 µW.

Fig. 6 displays the evolution of the relative change of transmittance for various repetition rates above 10 MHz. Interestingly, the measured damage threshold is nearly independent of the repetition rate in the studied high-repetition-rate regime. Moreover, the damage thresholds are very close, if not identical, to the measured continuous-wave threshold. This suggests that a heat-accumulation effect rather than a single-pulse phenomenon is causing the damage.

However, even though the fluence ("single-pulse-energy density") has minimal to no impact on the damage threshold in this regime, it does have an impact on the damage rate with a clear tendency to increase with increasing fluence.

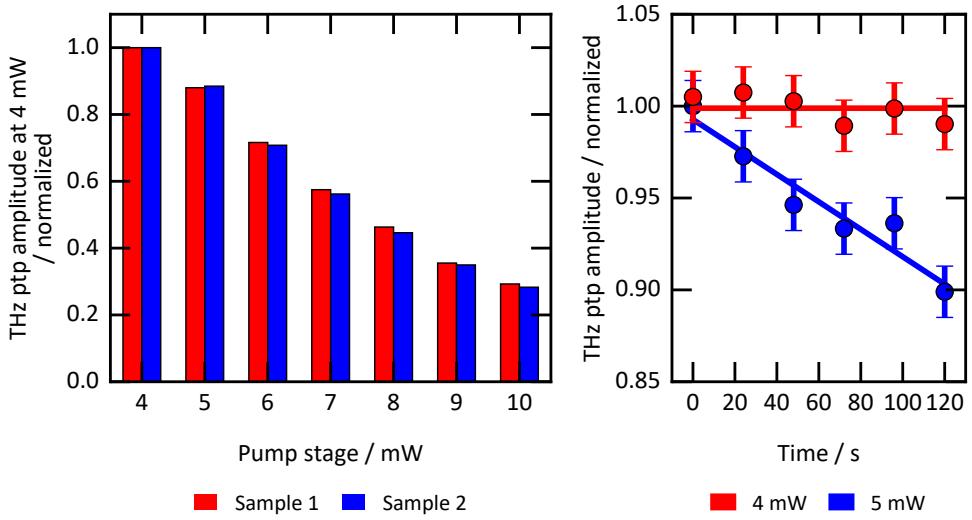

Fig. 3. Terahertz peak-to-peak (ptp) amplitude at a 4 mW reference level after each pump stage (left) and the temporal evolution at 4 and 5 mW (right). Beginning with the 5 mW pump stage, an irreversible decrease is evident.

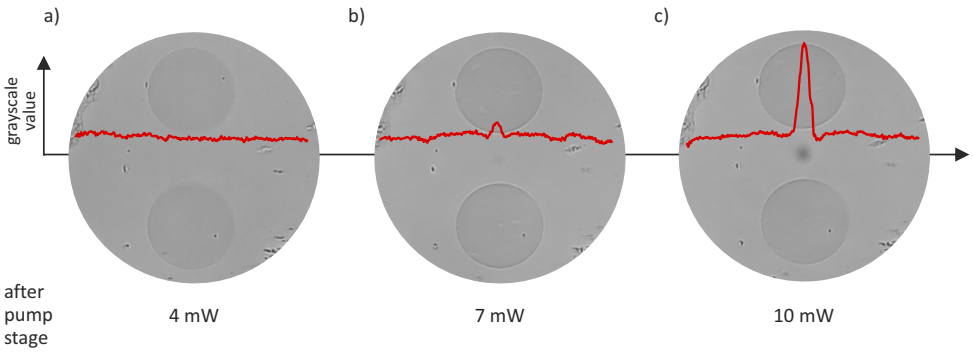

Fig. 4. Microscopy images of a fiber-tip STE's end facet after three continuous-wave pump stages. The grayscale values corresponding to central line scans are depicted in red at equal scale. While the fiber-tip STE exhibits no signs of destruction after the 4 mW pump stage (a), a faint darkening becomes noticeable within the region of the fiber's core after the 7 mW pump stage (b). After the 10 mW pump stage, the darkening is highly pronounced (c).

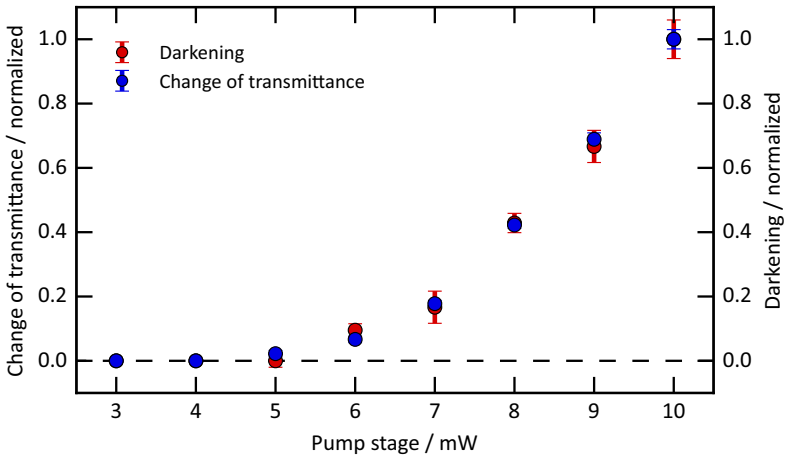

Fig. 5. Comparison of the optical-microscopy-detected darkening and the change of infrared transmittance averaged over three continuous-wave-irradiated samples. The change of transmittance and the quantified darkening evolve nearly identically. The damage onset (defined by a transmittance increase of 10 µW) is observed around 5 mW.

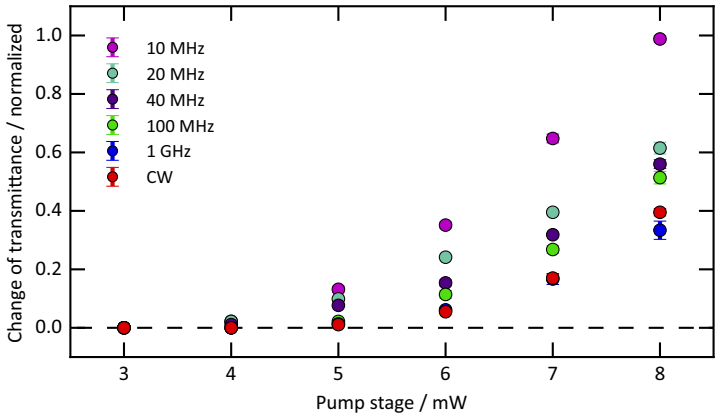

Fig. 6. Relative change of transmittance for various repetition rates. The damage onset (defined by a transmittance increase of 10 µW) remains nearly independent of the repetition rate. However, the damage rate increases with increasing repetition rate as the fluence rises.

3.4. Fluence thresholds

Fig. 7 shows the fluence threshold over the entire repetition-rate range. To calculate the fluence, we assumed a Gaussian beam profile with a $1/e^2$ mode field radius ω of 5.75 μm (as specified by Fujikura Ltd. for the used polarization-maintaining single-mode fiber "SM15-PS-U25D") which corresponds to an effective mode area $A_{\text{eff}} = \pi\omega^2 = 103.87\ \mu m^2$. The fluence is then defined as the ratio of pulse energy and A_{eff}. For each repetition rate, the pulse energy has been carefully determined by measuring the average optical power with a power meter and analyzing the amplified spontaneous emission (ASE) background noise using a calibrated fast photodiode.

Remarkably, the repetition-rate range is split into two distinct regimes: a low-repetition-rate regime being governed by a constant fluence threshold (blue) and a high-repetition-rate regime being governed by an antiproportional fluence dependence (red). The red dashed line represents the measured continuous-wave average-power threshold extrapolated to the entire repetition-rate range. Most notably, the fluence thresholds remain strikingly consistent with the continuous-wave threshold down to a repetition rate of approximately 4 MHz. Below, the established regime with a constant fluence threshold is entered.

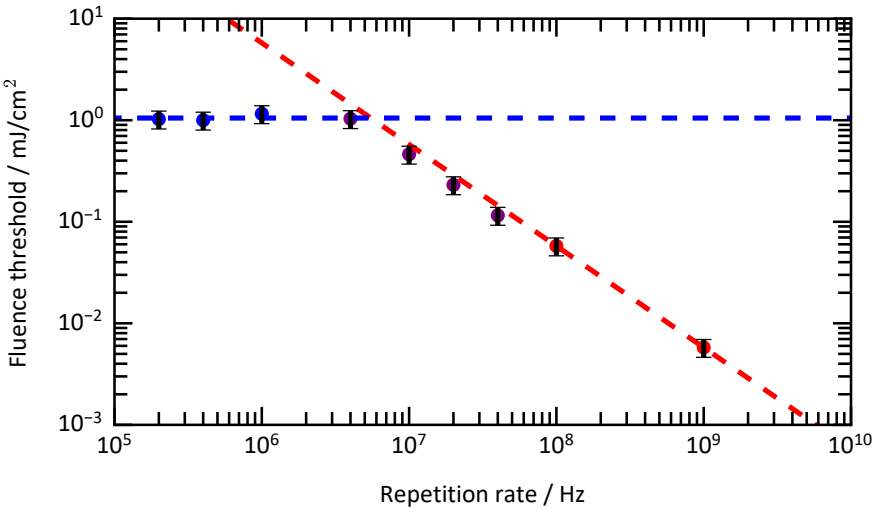

Fig. 7. Extracted fluence threshold in dependence on the repetition rate. Two clearly distinguishable regimes are apparent: a high-pulse-power low-repetition-rate regime characterized by a constant fluence threshold (blue), and a low-pulse-power high-repetition-rate regime characterized by an antiproportional fluence-dependence ("average-power threshold"). The red dashed line corresponds to the measured continuous-wave average-power threshold extrapolated to the entire repetition-rate range by applying an inverse proportionality.

3.5. Thermodynamics and nanoscopy

3.5.1. Theory

The two regimes indicate two different damage processes being at play. In the low-repetition-rate regime, the period duration between two subsequent pulses is long enough for the material system to cool down to its initial state again. As a result, heat accumulation does not happen and only single-pulse interactions are responsible for the material damage. Hence, the damage threshold is directly linked to fluence and peak power.

On the contrary, in the high-repetition-rate regime, the period duration is too short for the material system to cool down to its initial state again. Consequently, heat accumulates and the temperature equilibrates at a new average-pump-power-dependent level. Once a specific temperature threshold is surpassed, the system's thermal energy is high enough to drive inter-layer diffusion of atoms, especially between the FeCoB- and the Pt-layer. In other words, the high temperature causes the FeCoB- and Pt-layer to alloy. As shown in a recent study that compares the terahertz emission of Fe/Pt bilayer STEs across various degrees of alloying [34], the electrical properties of the bilayer and alloyed heterostructure differ drastically with the result that the terahertz emission is almost entirely canceled for the fully alloyed phase. To test this theory of temperature-driven inter-layer diffusion, we performed AFM, infrared s-SNOM, and STEM measurements for a pristine and a cw-destroyed sample, respectively.

3.5.2. AFM and s-SNOM

Fig. 8 a) shows the AFM images for a pristine and a cw-destroyed sample (comparable to the samples shown in Fig. 4 a) and c)). The measured topology reveals an irreversible expansion of more than 3 nm with a spatial profile mapping the Gaussian pump-mode field. Anticipating the STEM measurements below, the expansion does not originate from an enlargement of the STE

heterostructure, but from the glass substrate. This observation hints at a prior transient rise in temperature as the material properties of glass depend on its thermal history.

Moreover, in addition to the permanent substrate expansion, the optical properties have been altered indicating a change in chemical composition. The infrared s-SNOM measurements in Fig. 8 b) resolve this chemical transformation spatially and provide another clear mapping of the Gaussian pump-mode field.

Combining these two findings, the temperature-driven nature becomes evident.

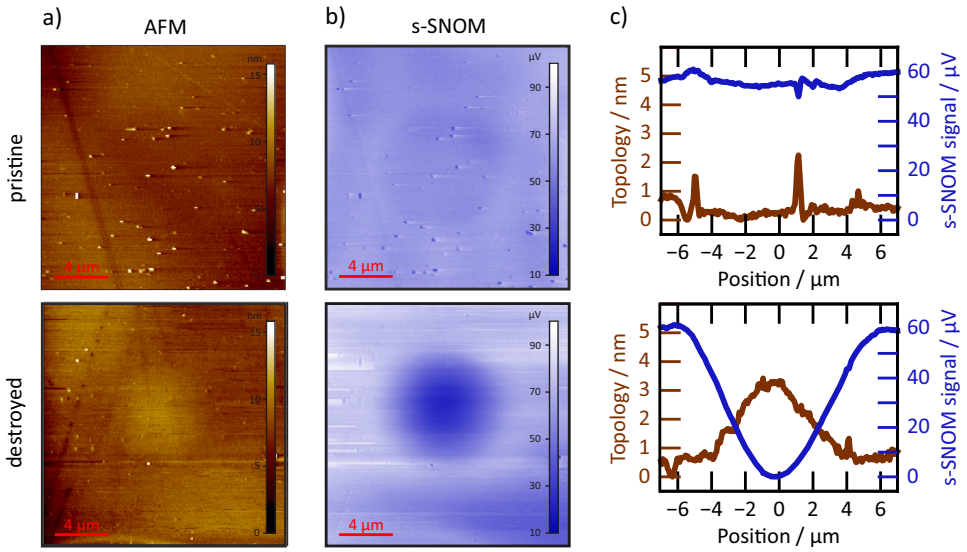

Fig. 8. AFM and infrared s-SNOM measurements for a pristine and a cw-destroyed single-mode fiber-tip STE. a) The AFM images of the pristine and destroyed samples show a similar surface roughness. However, for the destroyed sample, a substrate expansion within the fiber's core region becomes visible. b) A comparison of the infrared s-SNOM images provides an even higher contrast indicating a change in chemical composition. In the image of the pristine sample, the fiber's core is slightly visible as the difference in refractive index yields a difference in reflectance. c) The line scans through the center reveal that both the topology (brown) and the s-SNOM signal (blue) of the destroyed sample map the Gaussian pump-mode field.

3.5.3. STEM

To complete the picture and verify the inter-layer diffusion, STEM measurements have been performed. Fig. 9 shows the resulting high-angle annular dark field (HAADF) and bright field images: In the pristine sample, the individual layers (W, FeCoB, and Pt) are distinguishable in both dark-field and bright-field measurements. However, in the destroyed sample, the heterostructure is altered and individual layers are barely, if at all, distinguishable. Fig. 9 c) shows the spatial distribution of W, FeCoB, and Pt measured with energy-dispersive X-ray spectroscopy. It becomes apparent that the FWHMs of the FeCoB and Pt distributions along the out-of-plane direction are significantly increased for the destroyed sample compared to the pristine one. In other words, an inter-layer diffusion between the FeCoB- and the Pt-layer had taken place.

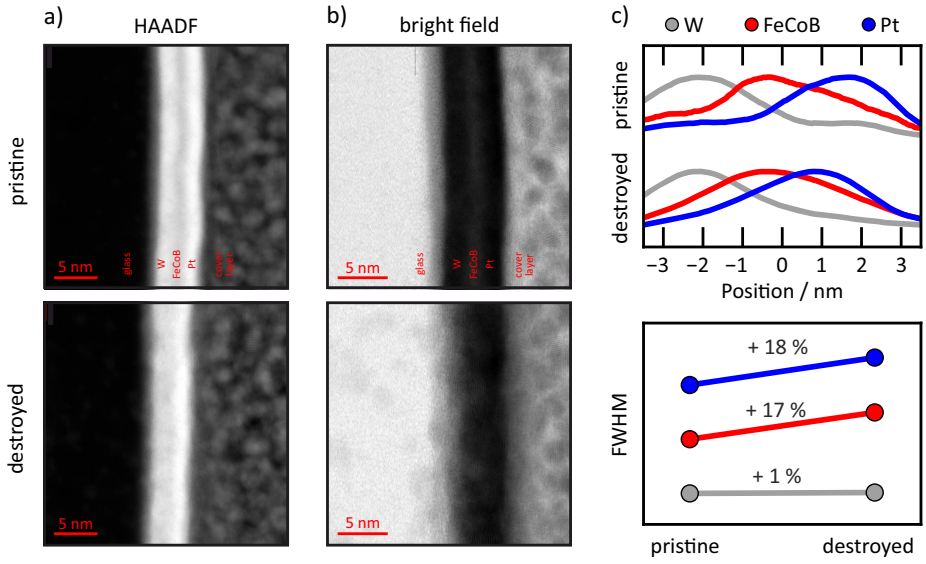

Fig. 9. Scanning transmission electron microscopy (STEM) measurements for a pristine and a destroyed single-mode fiber-tip STE. The pristine tri-layer heterostructure is visible in both dark-field (a)) and bright-field (b) imaging. In the destroyed sample, the tri-layer heterostructure is altered clearly and only barely, if at all, discernible in the dark field imaging. The individual layers' spatial distributions, measured with energy-dispersive X-ray spectroscopy, support the theory of an inter-layer diffusion between the FeCoB- and Pt-layer as the FWHMs are significantly increased for the destroyed sample.

4. Conclusions

In summary, we presented a complete study of our single-mode fiber-tip STEs' optical damage threshold covering the kilohertz, megahertz, and gigahertz repetition-rate regimes as well as continuous-wave irradiation. Most importantly, we revealed the necessity of classifying the optical damage threshold of fiber-tip spintronic terahertz emitters into two regimes: a high-peak-power low-repetition-rate regime governed by a constant-fluence threshold, and a low-peak-power high-repetition-rate regime governed by an antiproportional fluence dependence ("average-power threshold"). In other words, we demonstrated continuous-wave-irradiation damage of STEs and could show that this cw-damage regime transitions to the known constant-fluence-damage regime only around 4 MHz for our single-mode fiber-tip STEs. Moreover, we provided a thermodynamic explanation of the processes at play and substantiated it with AFM, s-SNOM, and STEM measurements. While interpreting damage as a single-pulse phenomenon is applicable in the low-repetition-rate regime, a transition to a complex accumulated heat phenomenon occurs as the repetition rate enters the megahertz regime. Consequently, above a specific threshold, a temperature-driven inter-layer diffusion of atoms is driven which causes the FeCoB- and Pt-layer to alloy. The resulting drastic change in electrical properties shuts down the optical-to-terahertz conversion.

These findings contribute to a better understanding of the current limitations of spintronic terahertz emitters and, thus, may have a significant impact on the design of future STEs. Some strategies to circumvent damage in certain free-space applications have already been demonstrated, either by cooling the STE [27] or reducing the effective repetition rate through rotation of the STE [30].

5. Acknowledgement

The authors acknowledge funding from the Horizon 2020 European Union Research and Innovation program under FET-OPEN Grant agreement No. 863155 (S-Nebula) and Marie Skłodowska-Curie Grant agreement No. 860060 “Magnetism and the effect of Electric Field” (MagnEFi), as well as from the Deutsche Forschungsgemeinschaft (DFG, German Research Foundation) TRR 173 - 268565370 (SPIN+X, project B11), TRR 227 - 328545488 (Ultrafast spin dynamics, projects A05, B02, and B05), and SPP 2314 - KA 3305/5-1 (INTEREST, project ITISA). Furthermore, the authors acknowledge the project No. CZ.02.01.01/00/22_008/0004631 "Materials and Technologies for Sustainable Development," funded by the European Union and the state budget of the Czech Republic within the framework of the Jan Amos Komensky Operational Program and Czech Science Foundation 22-33060S. Moreover, the authors would like to thank the French RENATECH Network and the Nano Structuring Center at the RPTU Kaiserslautern-Landau for their technical support during the fabrication of the fiber-tip spintronic terahertz emitters.

6. Disclosures

The authors declare no conflicts of interest.

7. Data availability

The data that support the findings of this study are openly available at https://doi.org/10.5281/zenodo.10926629

References

1. B.B. Hu, X.-C. Zhang, D.H. Auston, and P.R. Smith “Free-space radiation from electro-optic crystals”, Appl. Phys. Lett. **56(6)** p.506-508 (1990).
2. J.A. Fülöp, S. Tzortzakis, and T. Kampfrath “Laser-Driven Strong-Field Terahertz Sources”, Adv. Opt. Materials **8(3)** 1900681 (2020).
3. H. Hirori, A. Doi, F. Blanchard, and K. Tanaka “Single cycle terahertz pulses with amplitudes exceeding 1 MV/cm generated by optical rectification in LiNbO3”, Appl. Phys. Lett. **98(6)** 091106 (2011).
4. X.-C. Zhang, X.F. Ma, Y. Jin, T.-M. Lu, E.P. Boden, P.D. Phelps, K.R. Stewart, and C.P. Yakymyshyn “Terahertz optical rectification from a nonlinear organic crystal”, Appl. Phys. Lett. **61(26)** p.3080-3082 (1992).
5. D. H. Auston and C. V. Shank “Picosecond Ellipsometry of Transient Electron-Hole Plasmas in Germanium”, Phys. Rev. Lett. **32** (1974).
6. D. H. Auston, K. P. Cheung, and P. R. Smith “Picosecond photoconducting Hertzian dipoles”, Appl. Phys. Lett. **45** (1984).
7. M. B. Ketchen, D. Grischkowsky, T. C. Chen, C-C. Chi, I. N. Duling III, N. J. Halas, J-M. Halbout, J. A. Kash, and G. P. Li “Generation of subpicosecond electrical pulses on coplanar transmission lines”, Appl. Phys. Lett. **48** (1986).
8. A. Dohms, S. Breuer, S. Keyvaninia, M. Gruner, L. Liebermeister, M. Schell, and R. B. Kohlhaas “Fiber-coupled THz transceiver based on rhodium-doped InGaAs with 6.5 THz bandwidth and up to 106 μW emitted THz power”, 48th IRMMW-THz (2023).
9. Y. Chen, Y. He, L. Liu, Z. Tian, X.-C. Zhang, and J. Daia “Plasma-based terahertz wave photonics in gas and liquid phases”, Photonics Insights **2(3)** (2023).
10. H. Hamster, A. Sullivan, S. Gordon, W. White, and R. W. Falcone “Subpicosecond, electromagnetic pulses from intense laser-plasma interaction”, Phys. Rev. Letters **71(17)** (1993).
11. D. Kuk, Y. J. Yoo, E. W. Rosenthal, N. Jhajj, H. M. Milchberg, and K. Y. Kim “Generation of scalable terahertz radiation from cylindrically focused two-color laser pulses in air”, Appl. Phys. Letters **108(12)** (2016).
12. I. Dey, K. Jana, V. Y. Fedorov, A. D. Koulouklidis, A. Mondal, M. Shaikh, D. Sarkar, A. D. Lad, S. Tzortzakis, A. Couairon, and G. R. Kumar “Highly efficient broadband terahertz generation from ultrashort laser filamentation in liquids”, Nat. Comm. **8(1)** (2017).
13. Z. Yu, N. Zhang, J. Wang, Z. Dai, C. Gong, L. Lin, L. Guo, and W. Liu “0.35% THz pulse conversion efficiency achieved by Ti:sapphire femtosecond laser filamentation in argon at 1 kHz repetition rate”, Opto-Electronic Advances **5(9)** (2022).
14. T. Kampfrath, M. Battiato, P. Maldonado, G. Eilers, J. Nötzold, S. Mährlein, V. Zbarsky, F. Freimuth, Y. Mokrousov, S. Blügel, M. Wolf, I. Radu, P.M. Oppeneer, and M. Münzenberg “Terahertz spin current pulses controlled by magnetic heterostructures”, Nature Nanotechnology **8** (2013).

15. E.T. Papaioannou, and R. Beigang "THz spintronic emitters: a review on achievements and future challenges", De Gruyter Nanophotonics **10** (2020).
16. Z. Feng, H. Qiu, D. Wang, C. Zhang, S. Sun, B. Jin, and W. Tan "Spintronic terahertz emitter", J. Appl. Phys. **129** (2021).
17. C. Bull, S.M. Hewett, R. Ji, C.-H. Lin, T. Thomson, D.M. Graham, and P. W. Nutter "Spintronic terahertz emitters: Status and prospects from a material perspective", APL Mater. **9** (2021).
18. T. Seifert, L. Cheng, Z. Wei, T. Kampfrath, and J. Qi "Spintronic sources of ultrashort terahertz electromagnetic pulses", Appl. Phys. Lett. **120** (2022).
19. R. Rouzegar, L. Brandt, L. Nádvorník, D.A. Reiss, A. Chekhov, O. Gueckstock, C. In, M. Wolf, T.S. Seifert, P.W. Brouwer, G. Woltersdorf, and T. Kampfrath "Laser-induced terahertz spin transport in magnetic nanostructures arises from the same force as ultrafast demagnetization", Phys. Rev. B **106** (2022).
20. I. Ilyakov, A. Brataas, T. V. A. G. de Oliveira, A. Ponomaryov, J.-C Deinert, O. Hellwig, J. Faßbender, J. Lindner, R. Salikhov, and S. Kovalev "Efficient ultrafast field-driven spin current generation for spintronic terahertz frequency conversion", Nat. Comm. **14** (2023).
21. U. Nandi, M. S. Abdelaziz, S. Jaiswal, G. Jakob, O. Gueckstock, S. M. Rouzegar, T. S. Seifert, M. Kläui, T. Kampfrath, S. Preu "Antenna-coupled spintronic terahertz emitters driven by a 1550 nm femtosecond laser oscillator", Appl. Phys. Lett. **115** (2019).
22. E. Th. Papaioannou, G. Torosyan, S. Keller, L. Scheuer, M. Battiato, V. K. Mag-usara, J. L'huillier, M. Tani, and R. Beigang "Efficient Terahertz Generation Using Fe/Pt Spintronic Emitters Pumped at Different Wavelengths", IEEE Transactions on magnetics **54(11)** (2018).
23. I. Ilyakov, N. Agarwal, J.-C. Deinert, J. Liu, A. Yaroslavtsev, L. Foglia, G. Kurdi, R. Mincigrucci, E. Principi, G. Jakob, M. Kläui, T. S. Seifert, T. Kampfrath, S. Kovalev, R. E. Carley, A. O. Scherz, and M. Gensch "Terahertz-wave decoding of femtosecond extreme-ultraviolet light pulses", Optica **9(5)** (2022).
24. T. Seifert, S. Jaiswal, U. Martens, J. Hannegan, L. Braun, P. Maldonado, F. Freimuth, A. Kronenberg, J. Henrizi, I. Radu, E. Beaurepaire, Y. Mokrousov, P.M. Oppeneer, M. Jourdan, G. Jakob, D. Turchinovich, L.M. Hayden, M. Wolf, M. Münzenberg, M. Kläui, and T. Kampfrath, "Efficient metallic spintronic emitters of ultrabroadband terahertz radiation", Nature Photonics **10** (2016).
25. R. Rouzegar, A.L. Chekhov, Y. Behovits, B.R. Serrano, M.A. Syskaki, C.H. Lambert, D. Engel, U. Martens, M. Münzenberg, M. Wolf, G. Jakob, M. Kläui, T.S. Seifert, and T. Kampfrath "Broadband Spintronic Terahertz Source with Peak Electric Fields Exceeding 1.5 MV/cm", Phys. Rev. Appl. **19** (2023).
26. S. Kumar, A. Nivedan, A. Singh, Y. Kumar, P. Malhotra, M. Tondusson, E. Freysz, and S. Kumar "Optical damage limit of efficient spintronic THz emitters", iScience **24** (2021).
27. T. Vogel, A. Omar, S. Mansourzadeh, F. Wulf, N. M. Sabanés, M. Müller, T. S. Seifert, A. Weigel, G. Jakob, M. Kläui, I. Pupeza, T. Kampfrath, and C. J. Saraceno "Average power scaling of THz spintronic emitters efficiently cooled in reflection geometry", Opt. Express **30(12)** (2022).
28. O. Gueckstock, L. Nádvorník, T. S. Seifert, M. Borchert, G. Jakob, G. Schmidt, G. Woltersdorf, M. Kläui, M. Wolf, and T. Kampfrath "Modulating the polarization of broadband terahertz pulses from a spintronic emitter at rates up to 10 kHz", Optica **8** (2021).
29. G. Lezier, P. Koleják, J.-F. Lampin, K. Postava, M. Vanwolleghem, and N. Tiercelin "Ultrafast Modulation of Polarization in Spintronic THz Emitters Enhanced by Field Induced Spin Reorientation Transition.", CLEO: Science and innovation **9** (2023).
30. A. Vaitsi, V. Sleziona, L. E. Parra Lopéz, T. S. Seifert, F. Schulz, N. M. Sabanés, M. Wolf, T. Kampfrath, and M. Müller "High-power operation of Spintronic Terahertz emitters for THz-field-driven scanning probe microscopy at MHz repetition rates", 48th IRMMW-THz (2023).
31. J. Cai, M. Dai, S. Chen, P. Chen, J. Wang, H. Xiong, Z. Ren, S. Liu, Z. Liu, C. Wan, M. Bai, and X. Wu "Terahertz spin currents resolved with nanometer spatial resolution", Appl. Phys. Rev. **10** (2023).
32. P. Kolejak, G. Lezier, G. Ducournau, J.-F. Lampin, N. Tiercelin, M. Vanwolleghem "Spintronic inverse spin hall photomixing beyond 1 THz", 48th IRMMW-THz (2023).
33. F. Paries, N. Tiercelin, G. Lezier, M. Vanwolleghem, F. Selz, M.-A. Syskaki, F. Kammerbauer, G. Jakob, M. Jourdan, M. Kläui, Z. Kaspar, T. Kampfrath, T. S. Seifert, G. von Freymann, and D. Molter "Fiber-tip spintronic terahertz emitters", Opt. Express **31(19)** (2023).
34. L. Scheuer, M. Ruhwedel, D. Karfaridis, I. G. Vasileiadis, D. Sokoluk, G. Torosyan, G. Vourlias, G. P. Dimitrakopoulos, M. Rahm, B. Hillebrands, T. Kehagias, R. Beigang, and E. Th. Papaioannou "THz emission from Fe/Pt spintronic emitters with $L1_0$-FePt alloyed interface", iScience **25** (2022).